Tribology International 186 (2023) 108596

Contents lists available at ScienceDirect

Tribology International

journal homepage: www.elsevier.com/locate/triboint

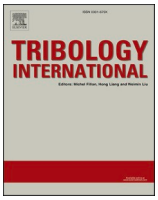

The effect of geometry on fretting fatigue test results in Al7075-t651 specimens with cylindrical contact

Vicente Martín, Diego Erena *, Jesús Vázquez, Carlos Navarro, Jaime Domínguez

Universidad de Sevilla, Escuela Técnica Superior de Ingenieros, Departamento de Ingeniería Mecánica y Fabricación, Camino de los Descubrimientos s/n, C.P., 41092, Spain

ARTICLE INFO

Keywords:
Fretting fatigue test
Cylindrical contact
Numerical model
Aluminium alloy

ABSTRACT

Fretting fatigue is a material damage phenomenon that produces damage on the contact surface, such as wear and surface cracks that can grow through the specimen. It is possible to reproduce the phenomenon in a laboratory using different geometries. In the absence of a common guide, this work studies the effect of different geometries of specimens and contact pairs on the fretting fatigue behaviour. This paper compares the results of a fretting fatigue test campaign made with cylindrical contact pairs made of AL7075-T651 alloy. In addition, 3D numerical models are developed to analyse the stress/strain fields and asses the total life. According to the experimental and numerical results, the differences of total life obtained between the geometries considered are negligible.

1. Introduction

The fretting fatigue phenomenon occurs when mechanical joints under pressure are subjected to varying loads that generate cyclic stress/strain fields and micro displacements between the surfaces in contact [1]. This produces different types of damage, such as wear, oxidation and the nucleation of cracks that can grow until the total failure of the parts. Fretting fatigue appears in many industrial applications, such as turbine blades or metallic cables [2]. Because fretting is very common in many engineering components, different authors have tried to reproduce the phenomenon under laboratory conditions. To do so, fretting fatigue has been reproduced in the laboratory using specimens and contact pads with simple geometries.

The American Society for Testing and Materials (ASTM) has compiled general requirements in the standard ASTM E2789 [3] as a guide for fretting fatigue tests. It provides recommendations for conducting tests and reporting the results and provides suggestions for developing them. The ASTM standard only recommends the alignment of the edges of the contact pad with the specimen, with the aim of minimising the concentration of pressure, but does not specify the specimen geometries at any point. For this reason, in the absence of a common guide, authors have studied specific geometries of specimens and contact pairs.

Examples of the tests, specimens and pad geometries used by different authors are listed below and organised by the type of contact. On the one hand, it is common to use flat pads pressed against flat surfaces. Some authors used bridge-type pads with thicknesses of 4 mm, 5.5 mm or 20 mm (Mutoh et al. [4], Kwon et al. [5] and Vantadori et al. [6]), while others authors, such as Hutson et al. [7] and Sun et al. [8], used simple flat pads with rounded edges with thicknesses of 10 mm and 5 mm or compared a flat pad with rounded edges and a flat pad with sharp edges at different angles, such as Mugadu et al. [9]. On the other hand, non-conformal contact is commonly studied with spherical and cylindrical pairs. Using a spherical pad against a flat surface is common in fretting fatigue analysis because it is the simplest and easiest type to assemble and align [10]. Vázquez et al. [11], Vantadori et al. [12] and Alfredsson et al. [13] used very different sphere radii ranging from 100 mm to 400 mm, and Venkatesh et al. [14] used smaller radii such as 12.7 mm or 25.4 mm. Finally, a cylindrical pad against a flat surface pair is probably the most commonly used type of contact. Szolwinski et al. [15] used specimens with square sections of 12.7 mm and different pad radii, Reza et al. [16] and Wang et al. [17] used a 50 mm pad radius and a 10 × 4 mm specimen section, Martín et al. used 100 mm radius pads on 10 × 8 mm specimen sections, and Vázquez et al. [19] used a section of 10 × 7 mm. Depending on the author, it is very common to use different specimen geometries for the same type of contact pair. For example, in the case of a cylindrical contact pair, there is no consensus among the authors on the choice of geometrical parameters, such as specimen and

* Corresponding author.
E-mail address: deg@us.es (D. Erena).

https://doi.org/10.1016/j.triboint.2023.108596
Received 26 January 2023; Received in revised form 3 May 2023; Accepted 11 May 2023
Available online 13 May 2023
0301-679X/© 2023 The Author(s). Published by Elsevier Ltd. This is an open access article under the CC BY-NC-ND license (http://creativecommons.org/licenses/by-nc-nd/4.0/).

pad thickness, specimen cross-section geometry or pad radius. Furthermore, for plane or cylindrical contact, the thickness of the specimen and the contact pad are usually the same, although in some cases these could be different from each other. For more details about the pads and specimen geometries used by different authors, the reader is encouraged to read the introduction of a previous work by the authors in which a review of 50 fretting papers with different contact pads and specimen geometries is depicted [20].

In the specific case of a cylindrical contact pair, which will be the object of analysis in this work, numerical analysis is usually simplified to 2D plane strain conditions with the objective of reducing the computational time [21,22]. However, these analyses do not allow for detecting differences in the stress distributions along the contact length (along the thickness of the specimen), which in some cases may be significant. This 2D assumption is also common in notched specimens. There have been some works about the 3D effects in notches or at the crack tip to highlight the importance of 3D models and analyse possible errors produced using that assumption [23–25]. In previous studies, the authors of this work numerically compared 3D and 2D stress fields in notches and fretting fatigue problems [26,27], Other authors used 2D or 3D models for the numerical analysis depending on the contact pair, cylindrical or spherical [28].

A recent author's work using 3D models to analyse fretting fatigue showed notable variations of stresses and strains close to the side border of the specimen surface, depending on the specimen cross-section or when the pad thickness was larger than the thickness of the contact surface of the specimen [20]. However, there is no evidence of producing different fatigue life results. To extend the analysis of the influence of geometrical parameters on the fretting fatigue behaviour, this paper experimentally and numerically analyses the effect on the total life produced by using different cross-section geometries of the specimen and different thicknesses for the specimen and the contact pad. To do so, a fretting fatigue test campaign was carried out. To understand the results of the tests carried out, 3D models are used to faithfully reproduce the actual stresses produced during fretting test. Finally, a fretting fatigue lifetime model is applied to estimate and compare with the experimental results.

This manuscript is organised as follows. First, the experimental campaign is presented, showing the test rig, the different specimens and contact pad geometries used as well as the parameters of the different tests carried out and the experimental results. Later, the numerical model used to analyse stresses, strains and fracture mechanics parameters is described, and some results are shown. Next, the fatigue model to simulate the fatigue crack initiation, propagation and total life is presented. Later, the results of the fatigue model are compared with the experimental results. Finally, some conclusions are shown.

2. Experimental campaign

The phenomenon of fretting fatigue can be reproduced under laboratory conditions using different types of devices that can apply normal and tangential loads on the pad while a bulk tension is acting on the specimen [29–32]. Fig. 1**a** shows a scheme for this type of test. Initially, a constant normal load, *N*, is applied to the contact pads. Usually, this load is kept constant throughout the test. Then, a cyclic axial load *P* is applied, and due to the stiffness of the pad supports and friction, a tangential contact load, *Q*, appears in the opposite direction to load *P*. The fretting fatigue device used in this work is the apparatus shown in Fig. 1**b** [33].

The material used for pads and specimens in all tests was Al7075-T651. The chemical composition and the mechanical properties are shown in Table 1 and Table 2 [34]. Five measurements of the grain size were made to obtain a mean value of 47.8 μm and a standard deviation of 8.9 μm.

2.1. Specimens and contact pad geometries

Two specimen geometries were selected for the test campaign. In both cases, the geometries of the specimens are dog-bone type. Hereinafter, thickness will be referred to as the Z-axis dimension and width of the contact surface (axial length of the specimen) as the X-axis (see Fig. 2). The section of the first specimen geometry is rectangular (10 × 8 mm), as shown in Fig. 2a and Fig. 2b. The second specimen type has a section that is obtained by machining opposite sides of a cylinder, producing flat surfaces 8 mm wide (see Fig. 2c). In both specimen geometries, the contact faces have a thickness of 8 mm. Additionally, the distance between the contact faces is 10 mm, independent of the geometry.

For the contact pads, two different geometries were selected, but in both cases, the contacting surface is cylindrical with a radius of 100 mm. One geometry has the same thickness as the test specimen contact surface (see Fig. 2a and Fig. 2c), and the other geometry has a thickness of 16 mm (see Fig. 2b). The first pad and test specimen geometry combination, see Fig. 2a, is thoroughly used in fretting fatigue works [11,18] in which the test specimen and the contact pad have the same thickness. Henceforth, this combination is called "Type 1″. The second contact pair, shown in Fig. 2b, is referenced here as "Type 2″. In this type of contact pair, the test specimen section is the same as "Type 1″, but the

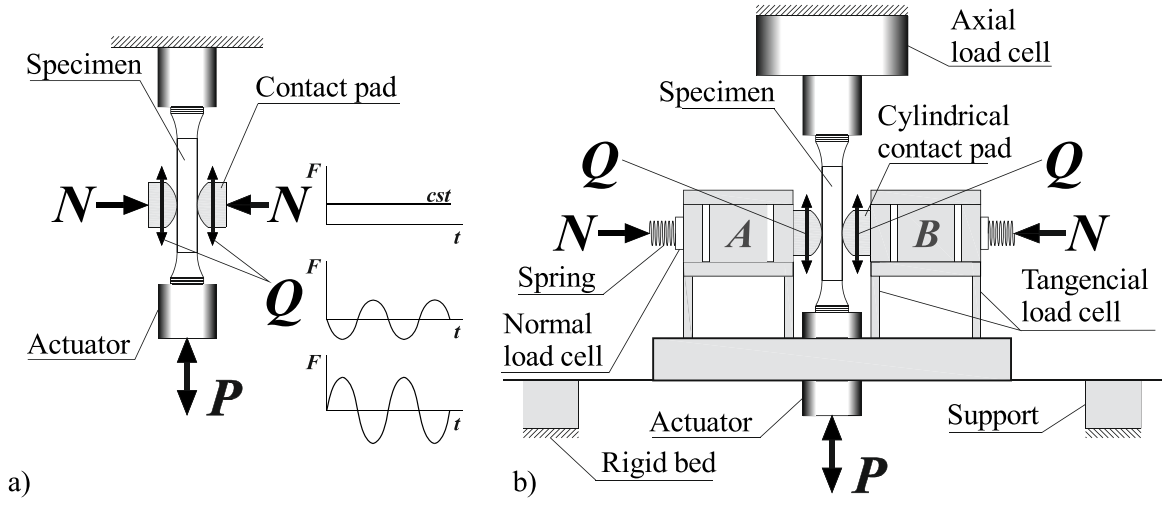

Fig. 1. a) Scheme of the fretting fatigue test with loads involved and the variation of these loads over time. b) Scheme of the fretting fatigue device used in the experimental campaign and the different parts involved.

Table 1
Chemical composition (% weight) for Al 7075-T651 [34].

%	Al	Zn	Mg	Cu	Fe	Si	Mn	Cr	Ti	Others
Max	91.4	6.1	2.9	2.0	0.5	0.4	0.3	0.28	0.2	0.05
Min	87.1	5.1	2.1	1.2	–	–	–	0.18	–	–

Table 2
Main mechanical and fatigue properties for Al 7075-T651.

Young's modulus[34]	E	71 GPa
Poisson's ratio[34]	ν	0.33
Yield strength[35]	σ_y	531 MPa
Tensile strength[35]	σ_u	600 MPa
Grain size[a]	d	47.8 μm
Strength coefficient[36]	σ'_f	1231
Ductility coefficient[36]	ε'_f	0.2634
Strength exponent[36]	b	-0.122
Ductility exponent[36]	c	-0.806

[a] Data obtained in our laboratory

contact pad has a thickness of 16 mm. It is important to remark that, for the second case, although the contact pads are larger than the specimen contact faces, the contact areas are limited by the thickness of the specimen contact faces. The third combination, "Type 3″, is the geometry used in [37] in which the test specimen surface has the same thickness as the contact pad but the test specimen section is not rectangular (see Fig. 2c).

The surface roughness is an important parameter used to define the contact conditions and compare with the finite element method (FEM) simulation that perfectly reproduces the radius and the flat surface. Three important roughness parameters are used to analyse the surface of the machined parts: the average roughness, *Ra,* is the mean value of all the profiles across the sample length; the maximum roughness depth, *Rt*, is the highest vertical distance between the highest peak and lowest valley in a selected sample length; and the mean roughness depth, *Rz*, which measures the distance between the five highest peaks and valleys in the sample length and then averages the value [38,39]. Computer numerical control (CNC) lathe and milling machines were used to manufacture the specimens and the contact pads with the finest and highest quality surface roughness that was offered. Table 3 shows the mean value of twenty measurements of these parameters and the standard deviation, σ_{Ri}.

2.2. Test campaign

The fretting fatigue test campaign was designed to produce fatigue lives in the range of 10^5 to 10^6 cycles, a regime in which the different stress gradients produced by the three contact pairs considered can have a noticeable effect. Two load combinations were selected, and these loads are shown in Table 4. In addition, the main Hertzian parameters assuming a cylindrical contact pair and plane strain conditions are also shown in Table 4. Both load combinations have the same normal load to

Table 3
Test specimen surface roughness before testing of Al7075-T651.

Measure	*Ra* (μm)	σ_{Ra}	*Rt* (μm)	σ_{Rt}	*Rz* (μm)	σ_{Rz}
X axis	0.29	0.05	2.14	0.31	2.05	0.37
Z axis	0.12	0.02	1.15	0.26	0.80	0.13

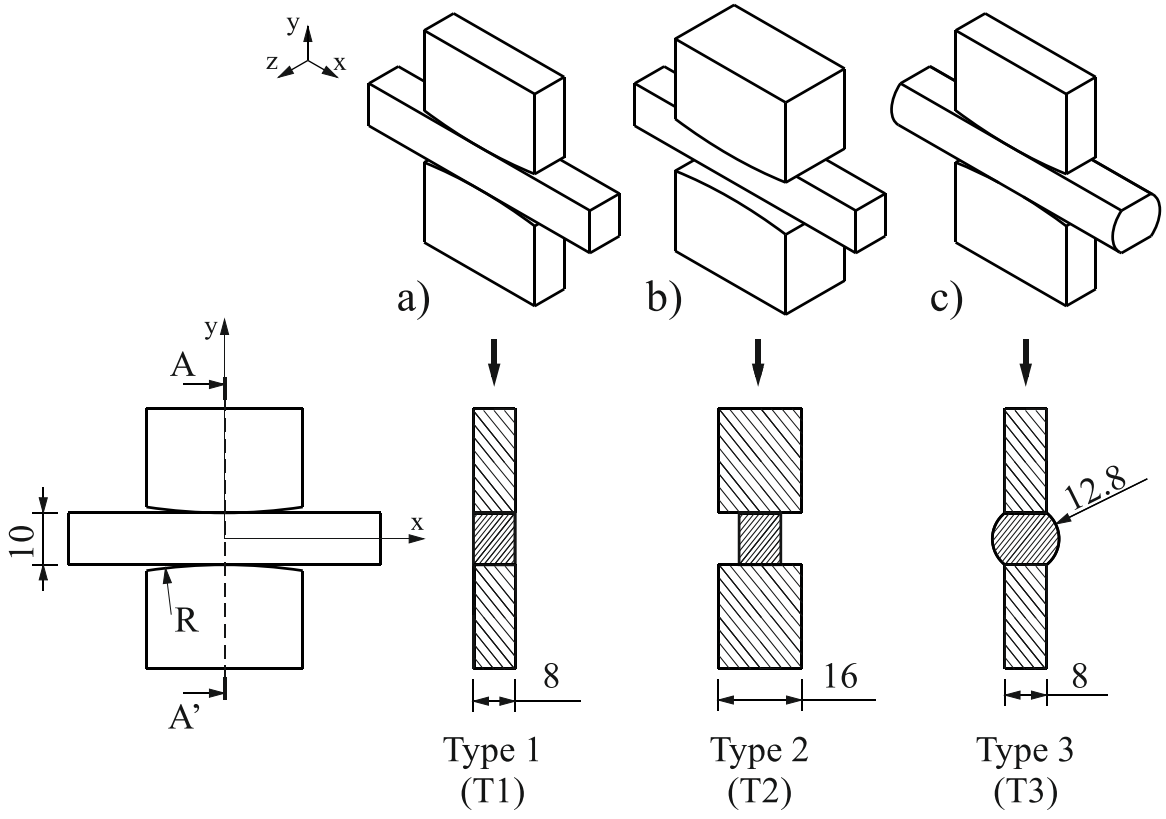

Fig. 2. Geometries of the different contact pairs used in this work.

Table 4
Test load combinations and related Hertzian parameters.

Load combination	N (N)	Q (N)	σ (MPa)	a_H (mm)	p_0 (MPa)	$\Delta\sigma_{xx}$ (x = a_H)
1	3690	970	70	1.23	239.3	602.73
2	3690	1250	90	1.23	239.3	695.93

reduce the difference between each load combination. In this way, the variation in the lives in the tests will depend on the tangential load and the bulk stress. Because the normal load is the same in both combinations, the Hertz contact half-width, a_H, and the peak contact pressure, p_0, will be the same, as shown in Table 4. The Hertzian parameters are calculated according to Eq. 1 to Eq. 5 [40].

$$a_H = \sqrt{\frac{8N' R(1-\nu^2)}{\pi E}} \tag{1}$$

$$p_0 = \frac{2N'}{\pi a_H} \tag{2}$$

$$c = a\sqrt{1 - \frac{Q}{\pi N}} \tag{3}$$

$$e = \frac{R\sigma(1-\nu^2)}{\pi E} \tag{4}$$

$$\Delta\sigma_{xx} = \sigma + 4\mu p_0 \frac{c}{a_H}\sqrt{\left(\frac{a+e}{c}\right)^2 - 1} \tag{5}$$

where N' is the normal load per unit length, c is the stick-zone semi-width, e is the eccentricity of the stick zone and μ is the coefficient of friction.

The specimens were manufactured with a 3-axis CNC lathe machine. Fig. 3 depicts the specimen section in which a small fillet can be observed at the corners. All specimen sections were analysed, and the mean radii observed were approximately 0.1 mm. To analyse whether this radius has a relevant effect on the total fatigue life, more specimens and contact pads were manufactured to guarantee sharp corners, and load combination 2 was applied with specimens and pads with edge fillets and sharp edges.

2.3. Experimental results

The results obtained in the test campaign are shown in Table 5. For each test, the normal load N, tangential load Q, bulk stress σ, and number of cycles to failure for the three contact pair combinations T1, T2 and T3 are shown. A total of 26 specimens were tested, 18 with fillet edges (Tests 1–6) and 9 with sharp edges (Tests 7–9). Due to some mechanical problems, test 9 with type 1 could not be used. Three specimens were tested for each load combination. In addition, the mean value and the standard deviation (SD), are calculated for each load combination and type of contact pair. It is possible to compare the deviation to know the dispersion of the results for the different types of tests. The range of SD values goes from 5.5% to 26.3% that is not a significant value in fretting fatigue tests. Analysing the mean values for each type it is possible to notice that the results are quite similar. Besides, if we consider also the SD it is possible to say that all the values lie in the same range. Finally, for load combination 2, it is possible to compare the cases with and without fillet, noticing that the mean values are slightly larger for the sharp edges. However, the differences taking into account the SD are substantially smaller. Therefore, we can say that the effect of the fillet is negligible in terms of total fatigue life and thus eliminating a variable from the problem.

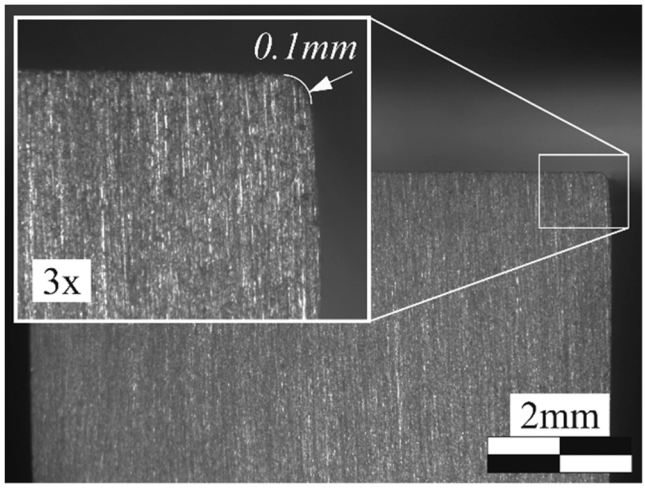

Fig. 3. Radius measured in the cross section of a specimen to analyse the corners.

Fig. 4 Shows two graphs with the results for load combinations 1 and 2. The results of the three different types of contact pairs are shown on each graph. The life results shown on the graph for load combination 1, which produces the lowest stresses, show more dispersion than load combination 2, with higher stresses, as usual in fatigue. Fig. 5 shows the comparison between the specimens manufactured with a radius of 0.1 mm and the improved specimens that have sharp corners. It is possible to see how the improved specimens have slightly higher lives in two of the three cases, T1 and T2. The contact pair T2 tests with sharp corners have similar lives to the specimen with a radius. Comparing the mean life values for different contact pairs for each load combination in Fig. 4 and Fig. 5, it can be said that although there is a certain tendency, with T3 producing the highest life and T2 the lowest, the differences in the average for each load combination are inside the scatter band of tests carried out with the same group. Furthermore, the tendency changes in the case of pads and specimens with sharp corners, where it is the opposite.

The fracture surfaces of the specimens were analysed to observe the crack evolution and possible differences due to the geometry. Fig. 6 shows the fracture surface of one specimen of each type of contact pair, as well as the scar produced in the contact zone. Regarding the scar, it can be seen that T1 and T3 produce a near rectangular scar, as would be the theoretical one in the case of uniform distribution of contact stress along the contact length. However, combination T2 produces a scar that is narrower in the central zone as a consequence of the higher contact pressure on the free faces of the contact zone and lower on the central part, as shown in [20]. Analysing the fracture surfaces, following the larger crack evolution (governing crack), on the left side for types 1 and 2 and on the right side for type 3 of the surface image in Fig. 6, it can be seen that there are several initiation points. The coalescence of these cracks creates the main crack, which finally produces the failure. In order to understand the crack evolution, it is interesting to analyse the crack that did not produce the failure (right side for Type 1 and 2 and left side for Type 3). In the case of combination T2 (Type 2), although cracks initiated first close to the corners, after some growth, they merged with other surface cracks into a main crack. This does not occur with the rest of the cases, since a perfectly straight crack front is observed.

3. Numerical model and results

The three test configurations used in the experimental campaign were modelled in Ansys software. Taking advantage of the symmetry planes, only half of one contact pair is considered. The models are 3D to capture the variation in stress/strain fields along the thickness of the assembly, especially at the two free surfaces of the specimens, where singularities are expected [20]. To reproduce the actual loading history in the fretting tests, loads are applied in three steps (see Fig. 7a). The first

Table 5
Fretting fatigue loads and life of tests.

		N.º	*N* (N)	*Q* (N)	*σ* (MPa)	*N (cycles) Type 1*	*N (cycles) Type 2*	*N (cycles) Type 3*
Load comb. 1	Fillet edges	1	3690	970	70	419457	360335	653849
		2	3690	970	70	336715	256102	395894
		3	3690	970	70	425215	472956	380768
	Mean					393795.7	363131	476837
	SD					10.3%	24.4%	26.3%
Load comb. 2	Fillet edges	4	3690	1250	90	187784	122691	185858
		5	3690	1250	90	168810	131924	199338
		6	3690	1250	90	165763	180630	212862
	Mean					174119	145081.7	199352.7
	SD					5.6%	17.5%	5.5%
	Sharp edges	7	3690	1250	90	187144	247086	218564
		8	3690	1250	90	223570	181965	211312
		9	3690	1250	90	-	228257	168948
	Mean					205357	219102.7	199608
	SD					8.9%	12.5%	10.9%

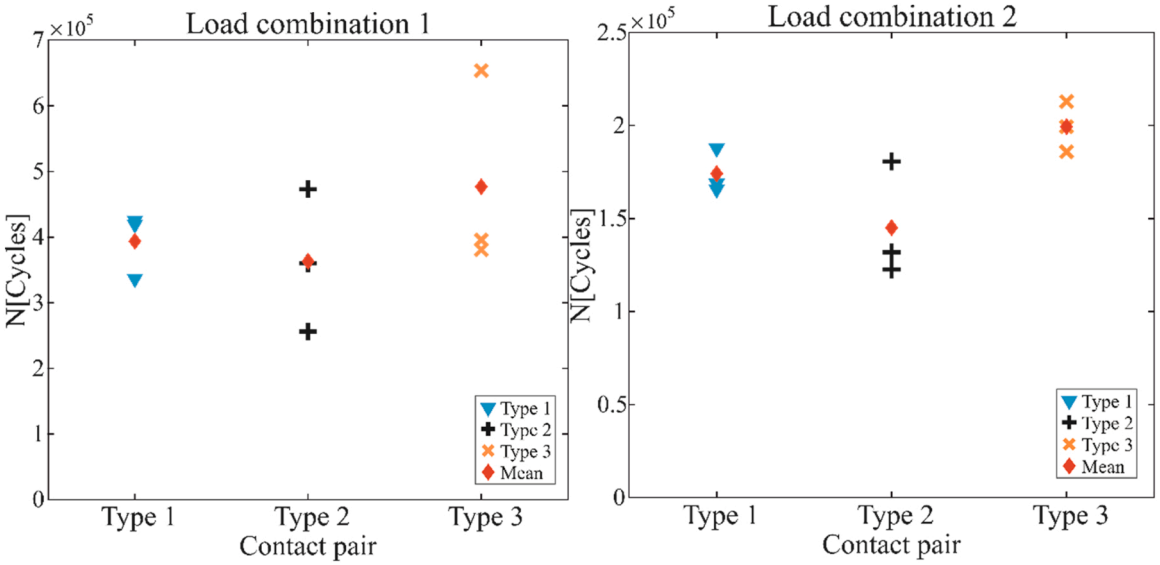

Fig. 4. Results graphs for load combinations 1 and 2 and each type of contact pair.

step applies the normal load, $N^* = N/2$. In our FEM model, the normal load applied to the contact pair is divided by 2 because due to the symmetry, only half of the contact pair is considered, and it is kept constant during the remaining steps. The second step applies the bulk stress, σ, to the right and the tangential force, $Q^* = Q/2$—again, the tangential load is divided by 2 due to symmetry—in the opposite direction. Finally, the third and last step removes σ and Q^* and again applies σ and Q^*, but now in opposite directions to that of the second step, thus reproducing a complete fretting cycle. The dimensions and relevant parameters of the FEM geometries are shown in Fig. 7b. In addition, a radius is performed at the external border of the specimen according to Fig. 3. In the present case, the radius is considered to be $0.1a_H$. The same radius is considered for the T1 and T2 configurations. Loads Q^* and N^* are applied to a master node that transfers these loads to all nodes lying on the top of the pad. The rotational movement of the master node is restricted. The bulk stress is applied to the right side of the specimen. The horizontal movement of the left side of the specimen is restricted, and symmetry conditions are applied to the remaining side. In the FEM model, a length of 10 a_H is taken for the test specimen (see Fig. 7**b**), a length that is enough to avoid the effect produced by the artificial boundary conditions applied at the left side of this element.

A linear elastic material behaviour is considered for both the contact pad and test specimen; although an elastic–plastic model can be considered, the different results between geometries are better analysed with a linear elastic behaviour, as the stresses involved are lower than the yield stress. The elastic modulus (Young's modulus) and Poisson's ratio are $E = 71$ GPa and $\nu = 0.33$, respectively, thus resembling the case in which the raw material of the contact pair is 7075-T651 aluminium alloy. To avoid artificial oscillation in the FEM contact stresses, a linear formulation for the solid and contact elements has been considered. Due to the 3D modelling, the number of elements increases significantly, and a good balance between computation time and accuracy should be achieved. In this sense, the minimum element size is approximately 40 μm and is located at the contact zone, obtaining sufficient accuracy for the objective of this work. The contact algorithm used in the simulations is the augmented Lagrangian method, which produces a good ratio between accuracy and CPU times. According to experimental values [41], the coefficient of friction, μ, has been fixed equal to 0.7, a high value that makes necessary the use of an asymmetric iterative solver to achieve numerical convergence.

Fig. 8 depicts the three models developed for the three assembly configurations, with a detailed view of the specimen to see the mapped and fine mesh at the contact zone. In addition, Fig. 8 shows the normal surface contact pressure distribution obtained for load combination 1. According to Hertz's theory, the maximum contact pressure assuming plane strain conditions, p_0, can be obtained with Eq. 2**,** where a_H is the contact semi-width (see Eq. 1) that only depends on the material constants, the normal load per unit length, N', and the pad radius, R.

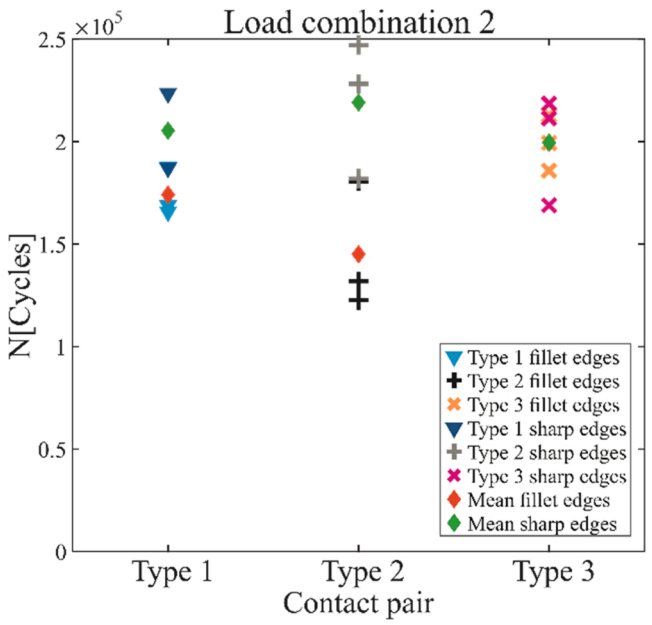

Fig. 5. Results graph for load combination 2 and each type of contact pair including sharp edge specimen results.

Therefore, for load configuration 1, the maximum contact pressure is approximately 240 MPa. This value is in good agreement with the results obtained from the 3D model and depicted in Fig. 8 for almost all the thickness of the specimens, which behave more or less in plane strain conditions. However, close to the specimen border, the actual behaviour is far from the plain strain, where the contact pressure significantly increases. This increase is almost negligible for the T1 configuration, reaching a maximum value of 290 MPa, but in the T2 configuration, this value is approximately 500 MPa. In configuration T3, we find an intermediate pressure of 355 MPa.

There are no analytical results for 3D fretting fatigue problems using a cylindrical pad and having the contacting bodies a finite size; that type of solution are only available for contacting bodies that can be modelled as half-planes and under plane stress and plane strain behaviour. Therefore, it is necessary to compare different sections of the 3D FEM model (at the free surface and the mid-thickness sections) with the analytical results available assuming plane stress and plane strain conditions. However, this comparison is not trivial and that is why there is a very extensive and detailed publication that deals with this problem, for a simple fretting case without bulk stress. Further details, comparisons and results in terms of the stress tensor at the contact zone and a more exhaustive validation can be found elsewhere [20]. For all these reasons the numerical results obtained are reasonable and in accordance with the analytical results available; therefore, the model could be validated.

3.1. Crack initiation phase

First, to analyse the crack nucleation behaviour, a plane perpendicular to the specimen longitudinal axis (Axis x, Fig. 7b) and located at the 2D theoretical contact trailing edge, the y-z plane with $x = a_H$, is analysed in terms of axial stress, $\sigma_{xx}(a_H,y,z)$. Although this parameter is very simple to analyse the crack initiation behaviour, it has been observed that in many situations, fretting cracks nucleate nearly perpendicular to this stress, especially in cylindrical contact pairs, leading to the same crack initiation point at the surface when a more sophisticated fatigue parameter is used [41]. Thus, the stress, σ_{xx}, is a simple and reliable parameter that can indicate the most damaged areas near the contact surface and is therefore more prone to the initiation of surface cracks.

As an example of the usage of the axial stress, the results for load combination 1 are depicted in Fig. 9 for time step 2, i.e., when a tensile axial load is applied to the test specimen. It can be noted that the axial stress at the contact edge is around four times the bulk stress applied, independently of the configuration. Fig. 9 shows that in general, the stress distributions obtained for all the configurations are different on the surface, noticing larger stresses for configuration T1, which at first could indicate shorter fatigue lives.

However, as mentioned, this is a very simple parameter that does not faithfully represent the fatigue behaviour, especially for the material beneath the surface, which has a multiaxial and non-proportional stress state along the fretting loading cycles. Therefore, it is more reasonable to compare the results between the three configurations analysing the evolution of a multiaxial fatigue damage parameter able to consider the non-proportional stress state. For the case of a cylindrical contact pair under fretting, former works have demonstrated that the Smith–Watson–Topper (SWT) parameter is a good choice to estimate crack initiation lives in fretting wear and fretting fatigue [15,42–47]. The indicated damage parameter is calculated on the basis of the stresses and strains of the specimen obtained from the 3D numerical model. To the best of our knowledge, that parameter cannot be measured in our case. First because it is not possible to measure stresses, and secondly, although strains can be measured, they can be only obtained at a free surface. Even more, in a fretting situation strains are extremely difficult to obtain due to the large gradients that appear in such small dimensions: in the order of hundreds of microns. The application of this critical plane parameter is easy in 2D models for obvious reasons. However, in the study that concerns us, it is impossible to simplify the 3D numerical model into a simplified 2D one. For this reason and supported by experimental data, it has been assumed that among all the critical planes, the most unfavourable one is the one that could contain a crack perpendicular to the surface, completely straight and emanating from the contact theoretical trailing edge. Therefore, the SWT parameter is calculated according to Eq. 6 (see Fig. 10**a**).

$$SWT = \sigma_{xx,\max}\frac{\Delta\varepsilon}{2} \tag{6}$$

where $\sigma_{xx,\max}$ is the axial stress at loading step 2 and $\Delta\varepsilon$ is the range of normal strain along the fretting cycle. However, the fatigue phenomenon, and in particular fretting fatigue, requires a deeper analysis considering what happens in the very near subsurface material—the fatigue process zone—since the initiation and early growth of fretting cracks is a process that depends on what happens in that process zone. Therefore, for a deeper comprehension, it is necessary to carry out an analysis below the contact surface to assess the more prone place for possible crack initiation along the test specimen thickness (Axis z, Fig. 10). For this reason, three different process zones are defined to analyse and compare the results in terms of the average SWT parameter in those zones. The first zone averages the SWT parameter at a quarter circular process zone centred at the assembly symmetry plane (see Fig. 10**b**). The shape of this process zone represents the size and shape of a possible initial crack with radius a emanating from the middle of the specimen (symmetry plane). The second process zone is at the corner of the specimen section and has the same shape as the former one but considering that the crack nucleates just at the fillet radius of configurations T1 and T2 and at the border of the contact zone in configuration T3. Finally, the third process zone is a rectangle beneath the surface, where the SWT parameter is averaged along the z-axis as a function of depth, as depicted in Fig. 10**b**. This last process zone represents an initial through crack with a length equal to the depth considered.

The results obtained are depicted in Fig. 10c, which shows the SWT evolution as a function of the length, a, of the process zone for load combination 1. Analysing Fig. 10c, it is clear that, close to the contact surface, differences are observed between the different process zones and assembly configurations. However, as the length of the process zone becomes larger (i.e., as we move away from the contact surface and inside the specimen), these differences dissipate and tend to the same

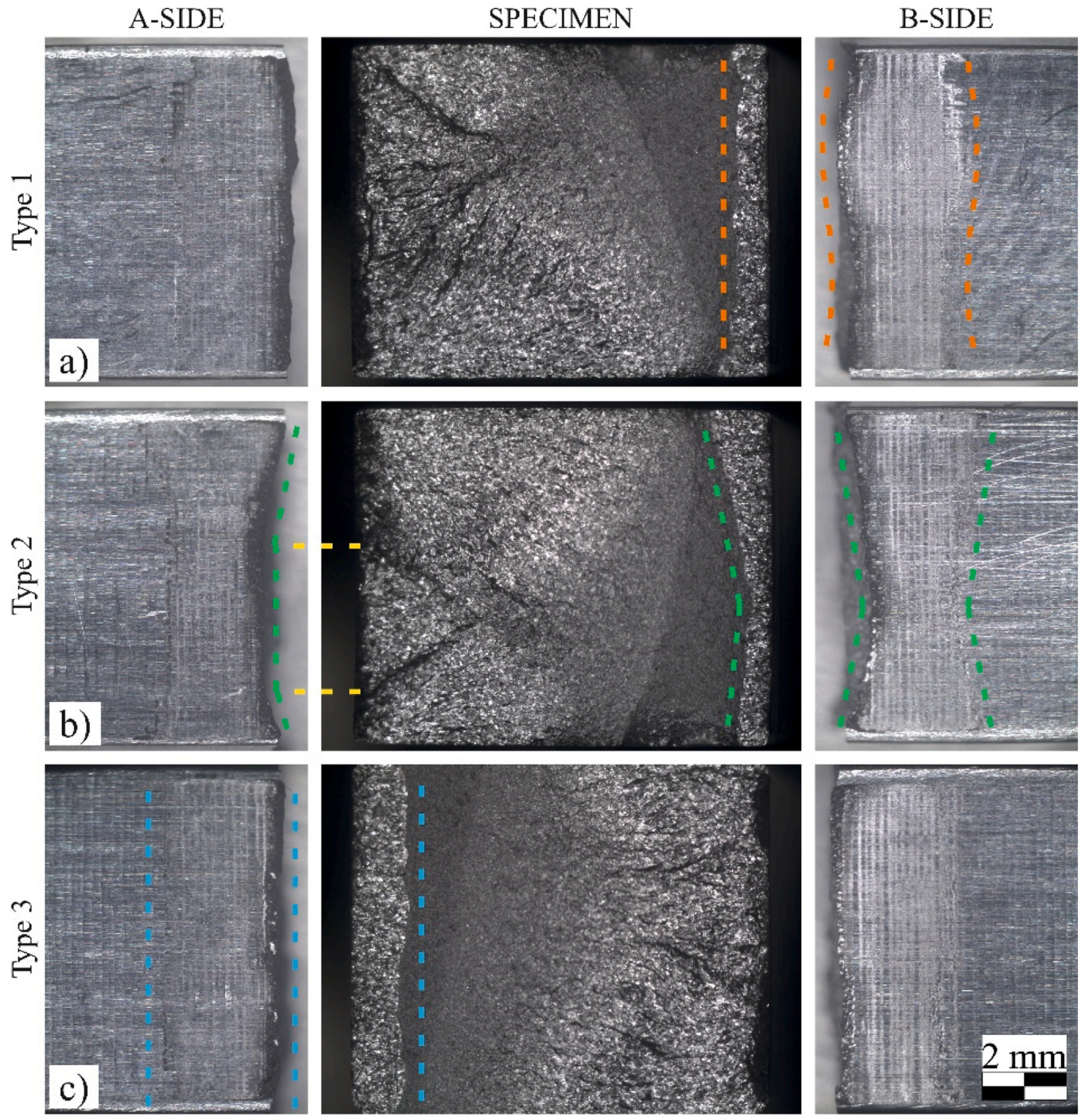

Fig. 6. Comparison of specimen crack surfaces and contact surfaces for each type of contact pair. All figures are plotted at the same scale.

value. If we analyse the global behaviour of the three configurations, independently of the process zone analysed, it is possible to see that the T1 and T2 configurations show larger values of the parameter close to the contact zone than the T3 configuration.

Independent of the configuration, the results show that just on the surface, the maximum value of the SWT parameter is obtained with the rectangular zone. However, close to the surface, a through crack does not make physical sense in our experience.

What is more remarkable is what happens from ~25 μm from the surface hereinafter. From this point, the most damaging curve for configuration T1 corresponds to the semi-elliptical crack at the surface. For the T2 configuration, the curves of the semi-elliptical crack at the edge and at the symmetry plane are the same, which indicates that the crack can start either from the edge or from an interior point. This is consistent with Fig. 6b, which shows how two cracks appeared first at the fillets but quickly also in the interior, joining later to form a through crack. Finally, in the T3 configuration, the semi-elliptical crack at the symmetry plane is also the most damaging, as occurs with configuration 1. This seems to indicate that the corner is no longer unfavourable, so one would expect several elliptical cracks that coalesce to form a perfectly trough crack front, as shown in Fig. 6a and 6c. Therefore, it is possible to narrow down the problem of simulating crack initiation and later growth, as will be seen later.

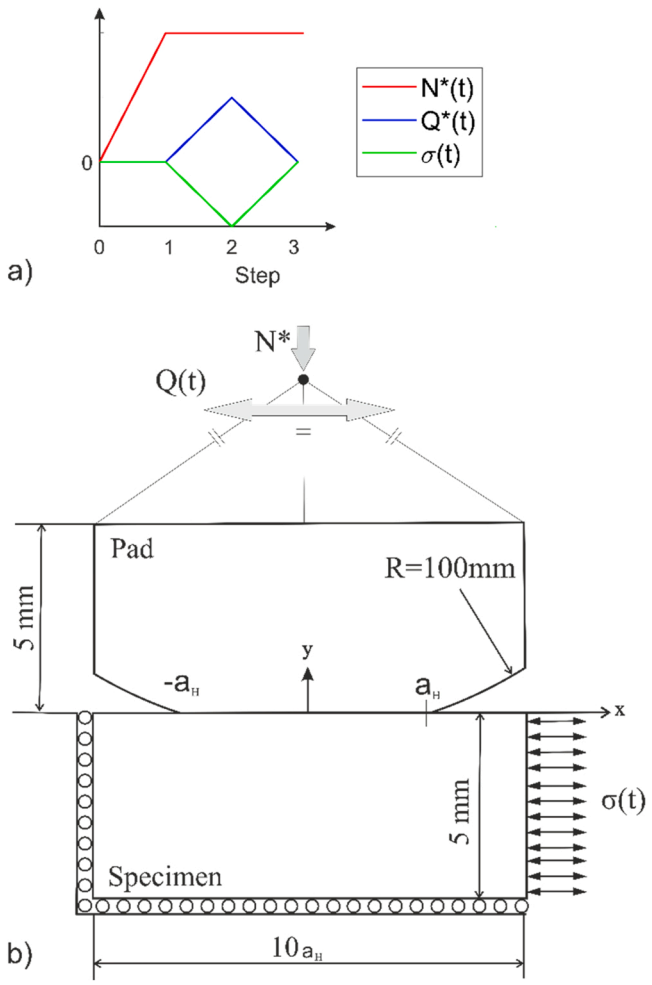

Fig. 7. a) Scheme of the load sequence; b) Main model parameters and boundary conditions.

3.2. Crack propagation phase

For each configuration and loading case, the mode I stress intensity factors (SIF) for cracks contained at the same critical plane of the former section (see Fig. 10a) are analysed. To do so, along this plane, the distribution of the axial stress, σ_{xx}, at load step 2, which is the normal crack opening stress, is used in conjunction with fracture mechanics software NASGRO [48]. Two different crack evolutions are considered in the analysis. In the first case, the crack is considered semi-elliptical and emanates from the middle of the specimen (SC case). In the second case, from the beginning, the crack is a through crack (TC case). In all cases, a bivariant formulation is used to obtain the mode I SIF. The results are depicted in Fig. 11 for load configuration 1 as an example. Blue lines are those corresponding to a surface semi-elliptical crack (SC) and it can be noted that the results, independently of the assembly type, are very similar. The results of this surface crack are valid up to a length of approximately 1 mm, as from this point, the crack becomes a trough crack. It is worth noting that this crack transition length of 1 mm is in good agreement with the photographs shown in Fig. 6. However, in this formulation, we consider a unique crack emanating from the middle thickness of the specimen, and the coalescence of several surface cracks into one is not modelled here. This assumption is slightly different from our experimental evidence (see Fig. 6) since it is observed that crack nucleation takes place at the same time at different points, which would mean that although the cracks are initially of an elliptical shape, they will quickly coalesce to form a trough crack, and this will occur before 1 mm depth [18]. As red lines show, the behaviour of a trough crack is different at short distances from the surfaces, yielding higher values of K_I if compared with a surface crack. Therefore, it is expected that the actual behaviour should be something between the two types of crack evolution considered here: SC and TC. Regarding the difference in behaviour between assembly configurations and for the same type of crack considered, the differences are negligible, with the exception of the T3 configuration for the TC case. It is worth noting that for the T3 configuration, the SWT parameter is the lowest for the first 100 μm, but from that length on, the values of K_I are the highest in the case of TC cracks and from approximately 400 μm for SC cracks. This fact can make that although the initiation may be slower with this configuration, later on the crack growth is faster, compensating in part for the initial differences.

4. Fatigue life prediction

Finally, a reliable fretting fatigue life prediction model previously developed by the authors [41,49–51] was applied to simulate the results of the test campaign. This model combines the crack initiation and propagation phases without defining a priori the crack length that defines the end of the initiation phase and the beginning of the crack propagation phase. Although the model can also address the crack orientation during the initiation and propagation phases [42], in the current work, it has been applied considering the curves obtained in the previous sections (see Fig. 10c). These curves have been obtained considering that the cracks will grow in a plane perpendicular to the specimen and containing the trailing edge. That is, we assume that the crack will be contained in the critical plane of Fig. 10a. Although a brief outline of how the model works is explained below, the reader can find a more detailed description elsewhere [42].

A summary of the model is shown in Fig. 12. The initiation phase analyses the number of cycles to initiate a crack of a certain length, a_i, by means of the stress/strain fields along the critical plane. In the present work, and due to the 3D nature of the bodies analysed, this is done for the 3 different process zones considered here (see Section 4.1). The number of cycles to generate this crack is obtained from a Coffin–Manson curve (ε-N) adapted to the SWT parameter (SWT-N). The result is a point of the curve (a_i-N_i) (see Fig. 12), which represents the number of cycles, N_i, needed to initiate a crack of length a_i as a function of a_i. Therefore, the curve is generated considering several discrete values of a_i.

The curve (a_i-N_i) represents the number of cycles required to initiate/nucleate a crack of length a_i. The number of cycles to nucleate a crack of length a_i will be obtained by means of the constant amplitude axial strain fatigue curve of the material, ε- N_T curve, where N_T is the number of cycle to failure. To achieve this goal, the ε-N_T curve of the material is expressed in terms of the SWT parameter (Eq. 7):

$$SWT = \frac{\sigma_f^{'2}}{E}(2N_T)^{2b} + \sigma_f^{'}\varepsilon_f^{'}(2N_T)^{b+c} \tag{7}$$

It is important to note that this curve represents the cycles up to what in tests was defined as failure, which is usually the complete fracture of the test specimen. This means that initiation and propagation cycles are joined in the term N_T. Nevertheless, for the objective of the current phase, it is necessary to construct a series of curves to obtain the number of cycles (N_i) required to nucleate a specific crack length (a_i) for each SWT level. The shape of these curves is represented in Fig. 13 and further developed in [42]. Therefore, to calculate the number of cycles to initiate a crack of length a_i in the fretting problem, the average value of SWT from the surface to a_i in this case is calculated and introduced in the corresponding curve in Fig. 13.

In the propagation phase, the number of cycles needed to propagate the previous initial cracks a_i up to failure are obtained by means of fracture mechanics-based methods. Integrating a crack growth law from an initial crack length, a_i, up to a crack length producing the test

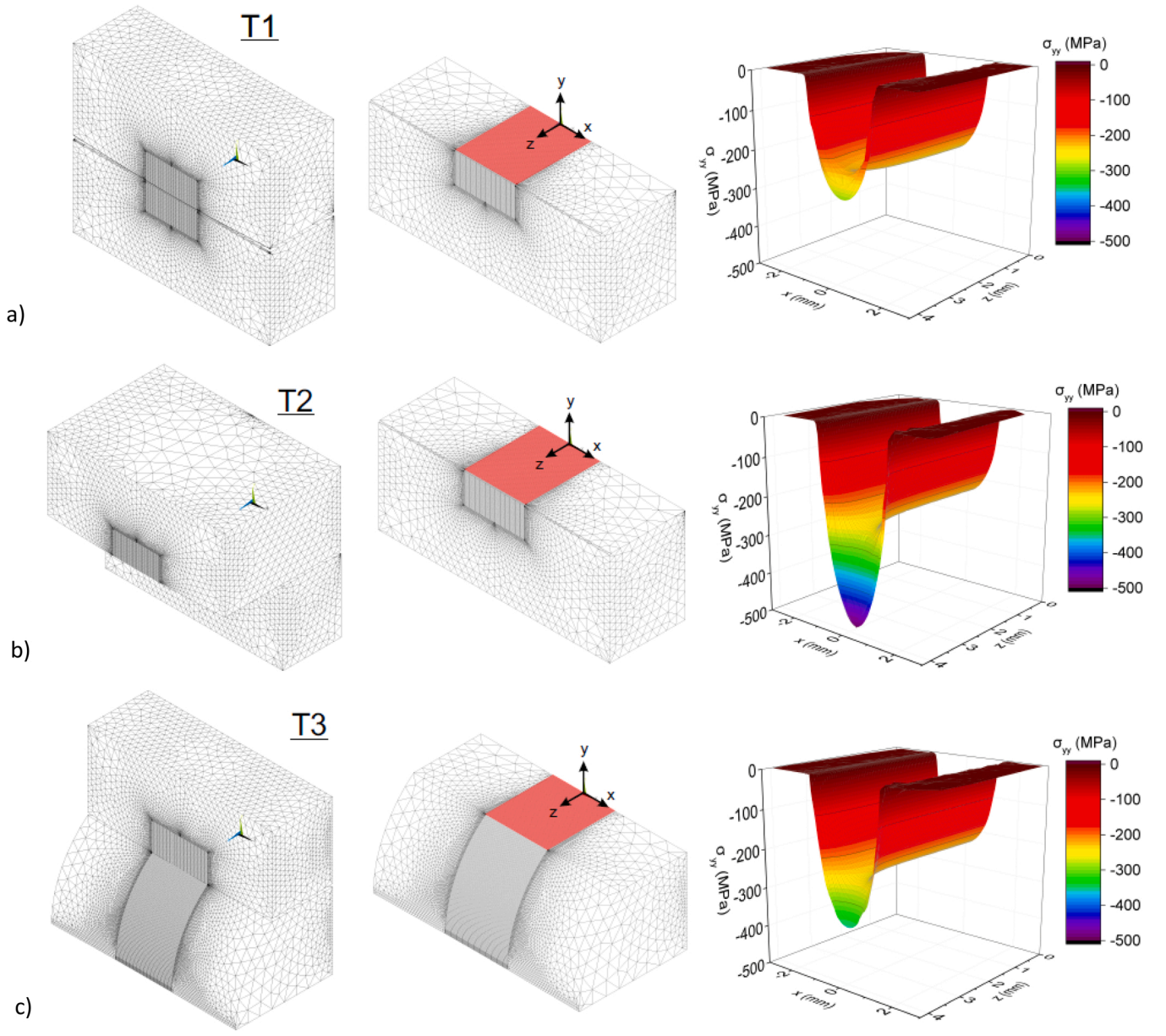

Fig. 8. Assembly and detail of the specimen FEM model and contact pressure distribution $\sigma_{yy}(x,0,z)$. a) T1 configuration, b) T2 configuration, c) T3 configuration.

specimen failure, the result is a point of the curve (a_i-N_p) (see Fig. 12). The curve is generated by repeating the process for all the previously defined a_i.

Finally, the sum of these two curves (a_i-N_i)+ (a_i -N_p) gives rise to the curve (a_i -N_T) (see Fig. 12). This curve should be understood as the total life estimated as a function of the crack length considered to delimitate the initiation and propagation phases, a_i. The minimum of the curve is considered the fatigue life estimation, $N_T{}^* = N_i{}^* + N_p{}^*$, since it is the most unfavourable and conservative value of all possible combinations, and $a_i{}^*$ is the crack initiation length. It can also be proven that for a tentative a_i smaller than $a_i{}^*$, the crack growth rate, defined as the slope of the curve, corresponding to (a_i-N_i) is higher than the one corresponding to (a_i -N_p). Above this point is the opposite.

The model applies for the load combinations and specimens previously described. The results are shown in Fig. 14. On the one hand, Fig. 14a depicts the fretting fatigue predictions considering a surface crack for the initiation phase (using the curve in Fig. 10c labelled Symm.), and then, for the propagation phase, an initial surface elliptical crack, that when growing, becomes a through crack (results of Fig. 11). On the other hand, Fig. 14b depicts the estimated lives considering the rectangular process zone and a through crack (now using the curve in Fig. 10c labelled Rect.).

Considering the scatter of the experimental results, the estimated fretting fatigue lives are reasonable. However, note that the results in which a fully through crack is considered from the beginning are more accurate. This may be because the coalescence of elliptical microcracks occurs very quickly and close to the surface, so it can be considered that there is only one through crack from the beginning.

In any case, the ultimate objective of this work was to check whether there is a substantial difference in the experimental fretting fatigue life as a function of the contact pair geometry used in the tests. The experimental results indicate that there is no appreciable difference, which agrees with the predictions made by the fretting fatigue model used here, especially if a through crack is considered. This is not to say that there are no differences between the contact stress/strain fields produced by the different geometries, but if there are, their influence is overshadowed by the dispersion of the life results.

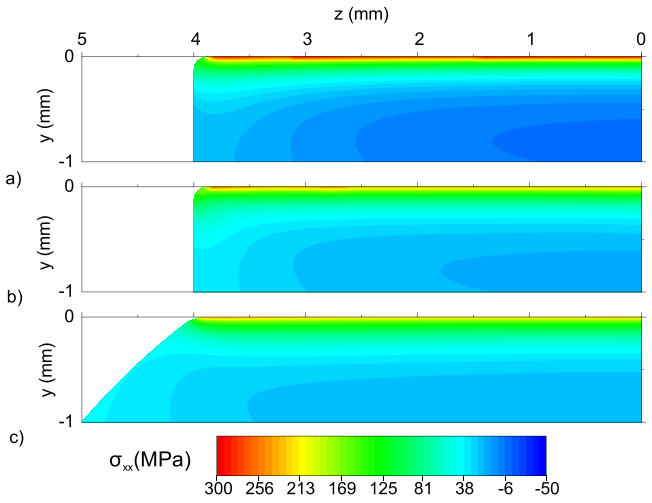

Fig. 9. $\sigma_{xx}(a_H, y, z)$ distributions for load combination 1. a) T1 configuration, b) T2 configuration, c) T3 configuration.

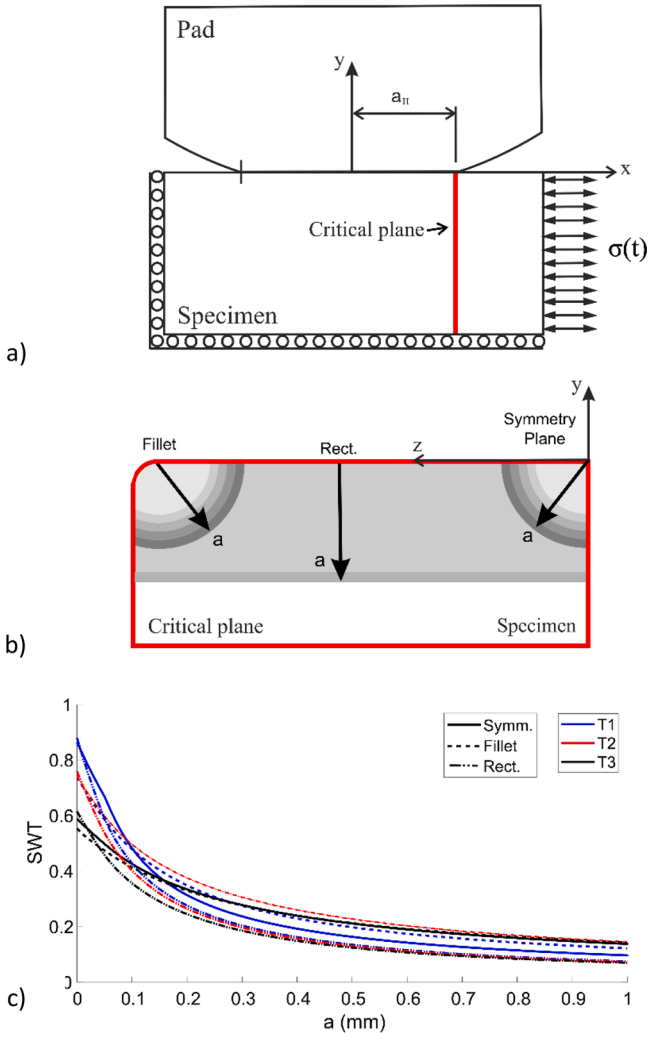

Fig. 10. a) Critical plane position, b) Process zones at the critical plane, c) Evolution of the SWT.

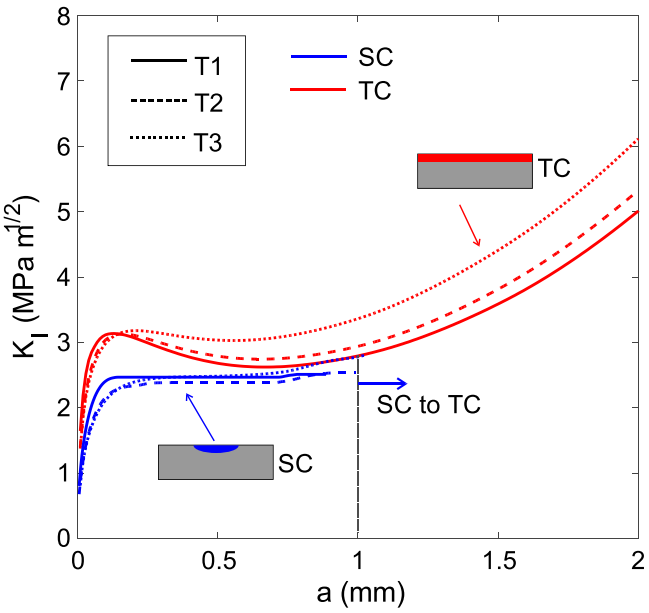

Fig. 11. SIF evolution for two types of cracks and loading configuration 1.

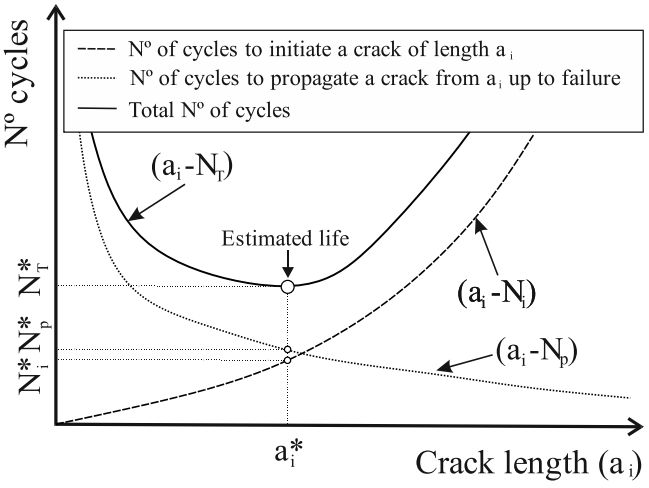

Fig. 12. Example of the curves obtained by applying the fatigue model.

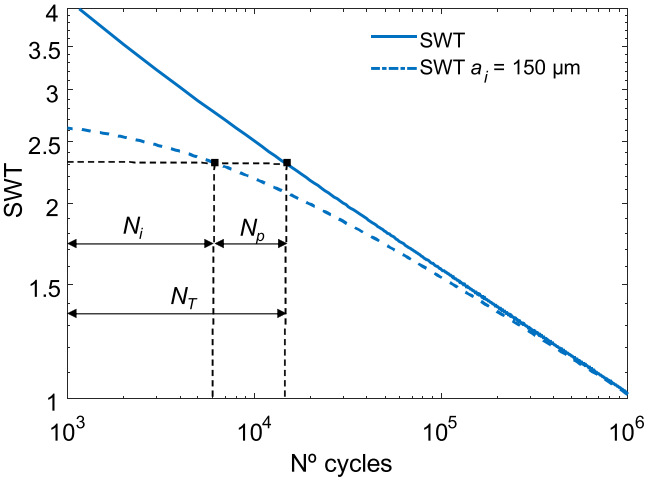

Fig. 13. Creation of initiation curves *SWT-N_i* in plain uniaxial fatigue.

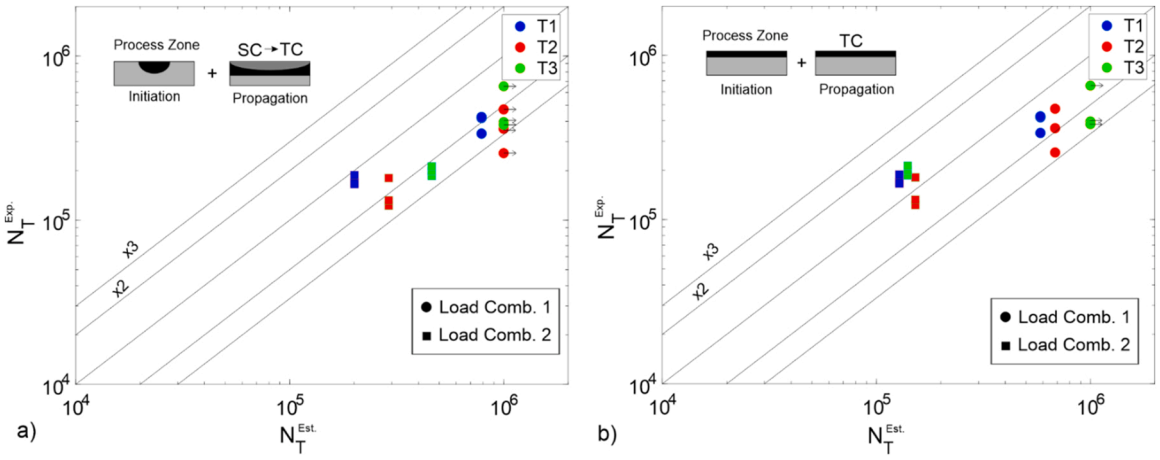

Fig. 14. Fatigue life estimation vs. fatigue test results: a) considering SC and b) considering TC.

5. Conclusions

This work has analysed the difference that can be expected in fretting fatigue tests with cylindrical contact when different specimens and pad geometries are used. Some experiments with different load combinations and different geometries have been carried out, as well as a fatigue model based on the numerical results. According to the numerical and experimental results, some conclusions are obtained. These conclusions can be divided into two groups: those obtained from the experimental results and those obtained by analysing the numerical model and the fatigue life predictions.

According to the experimental results, the different geometries tested have very similar lives for the same load combination. Differences in average for each load case are in the scatter bands of the lives obtained with each geometry. The tests with the specimens and contact pads with sharp corners have results that are also very similar to those obtained for specimens and pads with radii. Therefore, it can be said that, at least for the load cases considered here and the small radii used, the radii are not very influential on the lives. In addition, based on the mean values of the lives obtained for the different configurations and the dispersion of the results, it can be said that the results in terms of fatigue life are similar regardless of the type used.

A post-analysis of the test specimens shows that the different types of contact pairs have different fretting scars, as expected due to the different contact pressure distributions. Additionally, the crack front on the side of the cracks that does not produce the failure has different geometries. Specifically, for configuration T2, where cracks seem to initiate at the filleted edges. However, these corner cracks quickly merge with surface cracks creating a quasi-straight crack front. In configurations 1 and 3 this is not observed, so that the cracks grow equally and at the same rate regardless of the point on the surface, so that a straight crack front is generated quickly, from small elliptical cracks. These remarks show that the stress and strain distributions have variations between the different types of tests.

Regarding the numerical analysis, the results in terms of fatigue life prediction corroborate the experimental results. However, the results considering a through crack are better than those obtained assuming an elliptical crack. In the case of a through crack approximately 90% of the results fall on the scatter band of $\pm$ 2, which is a very good prediction in fretting fatigue. However, the fatigue model overestimates the life predictions for Type 3 assembly, although given the dispersion of the experimental results it is reasonable. Although slight differences could be found in terms of stress/strain fields close to the contact surface, they dissipate and balance as we move deep in the specimen.

Declaration of Competing Interest

The authors declare that they have no known competing financial interests or personal relationships that could have appeared to influence the work reported in this paper.

Data Availability

The authors do not have permission to share data.

References

[1] D.A. Hills, D. Nowell, Mechanics of Fretting Fatigue, Kluber Academic Publishers, Dordrech/Boston/London, ISBN: 0–7923-2866–3, 1994.Waterhouse R. Fretting fatigue. U.K: Applied science publishers; 1981. https://doi.org/10.1007/978–94-015–8281-0.

[2] Erena D, Vázquez Valeo J, Navarro C, Domínguez J. Fatigue and fracture analysis of a seven-wire stainless steel strand under axial and bending loads. Fatigue Fract Eng Mater Struct 2020;43(1):149–61.

[3] ASTM E2789. Standard Guide for Fretting Fatigue Testing. ASTM International; 2015.

[4] Mutoh Y, Tanaka K. Fretting fatigue in several steels and a cast iron. Wear 1988; 125:175–91. https://doi.org/10.1016/0043-1648(88)90201-3.

[5] Kwon J, Jeung H, Chung I, Yoon D, Park D. A study on fretting fatigue characteristics of inconel 690 at high temperature. Tribol Int 2011;44:148–1483. https://doi.org/10.1016/j.triboint.2010.11.006.

[6] Vantadori S, Abbasi F, Zanichelli A, Leonetti D, Pucillo GP, Majzoobi GH. Influence of normal load frequency on fretting fatigue behaviour by a critical plane-based approach. Int J Fatigue 2022;158:106724. https://doi.org/10.1016/j.ijfatigue.2022.106724.

[7] Hutson AL, Nicholas T, Goodman R. Fretting fatigue of Ti–6Al–4V under flat-on-flat contact. Int J Fat 1999;21:663–9. https://doi.org/10.1016/S0142-1123(99)00027-4.

[8] Sun S, Li L, He K, Yue Z, Yang W, Yu Z. Fretting fatigue damage mechanism of Nickel-based single crystal superalloys at high temperature. Int J Mech Sci 2020; 186:105894. https://doi.org/10.1016/j.ijmecsci.2020.105894.

[9] Mugadu A, Hills DA, Nowell D. Modifications to a fretting-fatigue testing apparatus based upon an analysis of contact stresses at complete and nearly complete contacts. Wear 2002;252:475–83. https://doi.org/10.1016/S0043-1648(02)00007-8.

[10] Wittkowsky BU, Birch PR, Domínguez J, Suresh S. Experimental investigation of fretting fatigue with spherical contact in 7075-T6 aluminum alloy. In: Current Technology and Practices. ASTM International; 2000. https://doi.org/10.1520/STP1367-EB.

[11] Vázquez J, Navarro C, Domínguez J. Experimental results in fretting fatigue with shot and laser peened Al 7075-t651 specimens. Int J Fat 2012;40:143–53. https://doi.org/10.1016/j.ijfatigue.2011.12.014.

[12] Vantadori Sabrina, Zanichelli Andrea. Fretting-fatigue analysis of shot-peened aluminium and titanium test specimens. Fatigue Fract Eng Mater Struct 2020;44 (2):397–409. https://doi.org/10.1111/ffe.13367.

[13] Alfredsson B, Cadario A. A study on fretting friction evolution and fretting fatigue crack initiation for a spherical contact. Int J Fat 2004;26:1037–52. https://doi.org/10.1016/j.ijfatigue.2004.03.010.

[14] Venkatesh TA, Conner BP, Suresh S, et al. An experimental investigation of fretting fatigue in Ti-6Al-4V: the role of contact conditions and microstructure. Metall Mater Trans A 2001;32:1131–46. https://doi.org/10.1007/s11661-001-0124-8.

[15] Szolwinski MP, Farris TN. Observation, analysis and prediction of fretting fatigue in 2024-T351 aluminum alloy. Wear 1998;221:24–36. https://doi.org/10.1016/S0043-1648(98)00264-6.
[16] Hojjati-Talemi Reza, Wahab Magd Abdel, De Pauw Jan, De Baets Patrick. Prediction of fretting fatigue crack initiation and propagation lifetime for cylindrical contact configuration. Tribol Int 2014;76:73–91. https://doi.org/10.1016/j.triboint.2014.02.017.
[17] Wang Can, Wang Dagang, Abdel Wahab Magd. Fretting fatigue lifetime estimation for heterogeneous material using critical distance with mesh control. Eng Fract Mech 2023;Volume 281:109092. https://doi.org/10.1016/j.engfracmech.2023.109092.
[18] Martín V, Vázquez J, Navarro C, Domínguez J. Fretting-fatigue analysis of shot-peened Al 7075-T651 test specimens. Met (Basel) 2019. https://doi.org/10.3390/met9050586.
[19] Vázquez J, Navarro C, Domínguez J. Analysis of fretting fatigue initial crack path in Al7075-T651 using cylindrical contact. Tribology Int 2017;108:87–94.
[20] Vázquez J, Erena D, Navarro C, Domínguez J. 3D contact effects in fretting fatigue tests. ISSN 0167-8442 Theor Appl Fract Mech 2022;Volume 118:103260. https://doi.org/10.1016/j.tafmec.2022.103260.
[21] Pinto AL, Cardoso RA, Talemi R, Araujo JA. Early crack orientation prediction methods under fretting fatigue loading including wear effects. Int J Fatigue 2022;Volume 161:106893. https://doi.org/10.1016/j.ijfatigue.2022.106893.
[22] Rangel D, Erena D, Vázquez J, Araújo JA. Prediction of initiation and total life in fretting fatigue considering kinked cracks. Theor Appl Fract Mech 2022;Volume 119:103345. https://doi.org/10.1016/j.tafmec.2022.103345.
[23] Berto F, Lazzarin P, Kotousov A, Pook LP. Induced out-of-plane mode at the tip of blunt lateral notchesand holes under in-plane shear loading. Fatigue Fract Eng Mater Struct 2011;35:538–55. https://doi.org/10.1111/j.1460-2695.2011.01647.x.
[24] Berto F, Kotousov A, Lazzarin P, Pook LP. On scale effect in plates weakened by rounded v-notches and subjected to in-plane shear loading. Int J Fract 2013;180:111–8. https://doi.org/10.1007/s10704-012-9796-x.
[25] Kotousov A, Lazzarin P, Berto F, Pook LP. Three-dimensional stress states at crack tip induced by shear and anti-plane loading. Eng Fract Mech 2013;108:65–74. https://doi.org/10.1016/j.engfracmech.2013.04.010.
[26] Navarro C, Vázquez J, Domínguez J. 3D vs. 2D fatigue crack initiation and propagation in notched plates. Int J Fatigue 2014;58:40–6. https://doi.org/10.1016/j.ijfatigue.2013.02.024.
[27] Vázquez J, Navarro C, Domínguez J. Two dimensional versus three dimensional modelling in fretting fatigue life prediction. J Strain Anal 2016;51(2):109–17. https://doi.org/10.1177/0309324715611510.
[28] Brito GA, Araújo R, Silverio RC, Araújo JA. A generalized ANN-multiaxial fatigue nonlocal approach to compute fretting fatigue life for aeronautical Al alloys. Tribology Int 2023;180:108250. https://doi.org/10.1016/j.triboint.2023.108250.
[29] Vincent L, Berthier Y, Dubourg MC, Godet M. Mechanics and materials in fretting. Wear 1992;153:135–48.
[30] Fenner AJ, Field JE. A study of the onset of fatigue damage due to fretting. Proc N E Coast Inst Eng Shipbuild 1960;76:183.
[31] Endo K, Goto H, Fukunaga T. Behaviours of frictional force in fretting fatigue. Bull JSME17 1974:647–54.
[32] Nishioka K, Hirakawa K. Fundamental investigation of fretting fatigue part 2. Fretting fatigue testing machine and some test results. Bull JSME 1969;12:180–7.
[33] Wittkowsky BU, Birch PR, Dominguez J, Suresh S. An apparatus for quantitative fretting testing. Fatigue Fract Eng Mater Struct 1999;22:307–20. https://doi.org/10.1046/j.1460-2695.1999.00145.x.
[34] Alloy 7075 Plate and Sheet: Alcoa Mill Products: SPD-10–037, 2001.
[35] Furuya Y, Nishikawa H, Hirukawa H, Nagashima N. Data sheets on low-and high-cycle fatigue properties of A7075-T6 (Al-5.6Zn-2.5Mg-1.6Cu) aluminium alloy, NIMS fatigue data sheet, No. 123. Tsukuba: Natl Inst Mater Sci 2017. https://doi.org/10.11503/nims.1187.
[36] Boller C, Seeger T. Materials data for cyclic loading: Low-alloy steels, Vol. 42. Elsevier; 2013.
[37] Nowell, D., (1988). An analysis of fretting fatigue. Doctor of Philosophy Thesis, Lincoln College, Oxford University, UK.
[38] Martín V, Vázquez J, Navarro C, Domínguez J. Effect of shot peening residual stresses and surface roughness on fretting fatigue strength of Al 7075-T651. Tribology Int 2020;142:106004. https://doi.org/10.1016/j.triboint.2019.106004.
[39] Effect of surface roughness and residualstresses J. Domínguez, J. Vázquez, and C. Navarro, in Fretting Wear andFretting Fatigue. Fundamental Principles and Applications, Tomasz Liskiewiczand Daniele Dini (Eds.), Elsevier, 2023, pp 335-381.
[40] Vázquez J, Navarro C, Domínguez J. A new method for obtaining the stress field in plane contacts. Int J Solids Struct 2012;Volume 49(Issue 26):3659–65. https://doi.org/10.1016/j.ijsolstr.2012.07.021.
[41] Vázquez J, Navarro C, Domínguez J. Analysis of fretting fatigue initial crack path in Al7075-T651 using cylindrical contact. Tribology Int 2017;108:87–94. https://doi.org/10.1016/j.triboint.2016.09.023.
[42] Erena D, Vázquez J, Navarro C, Domínguez J. A fretting fatigue model based on self-steered cracks. Theor Appl Fract Mech 2022;117:103144. https://doi.org/10.1016/j.tafmec.2021.103144.
[43] Szolwinski MP, Farris TN. Observation, analysis and prediction of fretting fatigue in 2024-T351 aluminum alloy. Wear 1998;221(1):24–36.
[44] Ding J, Sum WS, Sabesan R, Leen SB, McColl IR, Williams EJ. Fretting fatigue predictions in a complex coupling. Int J Fatigue 2007;29(7):1229–44.
[45] Chen JJ, Liu L, Li SX, Yu SR, He YN. Experimental and numerical investigation on crack initiation of fretting fatigue of dovetail. Fatigue Fract Eng Mater Struct 2018;41(6):1426–36.
[46] -Fridrici V, Fouvry S, Kapsa P, Perruchaut P. Prediction of cracking in Ti–6Al–4V alloy under fretting-wear: use of the SWT criterion. Wear 2005;259(1–6):300–8.
[47] Bhatti NA, Wahab MA. Finite element analysis of fretting fatigue under out of phase loading conditions. Tribology Int 2017;109:552–62.
[48] NASA. Fatigue crack growth computer program NASGRO Version 3.0—Reference manual. JSC-22267B, NASA, Lyndon B. Johnson Space Center, Texas, 2000.
[49] Navarro C, García M, Domínguez J. A procedure for estimating the total life in fretting fatigue, fatigue and fracture of engineering. Mater Struct 2003;26(5):459–68. https://doi.org/10.1046/j.1460-2695.2003.00647.x.
[50] Navarro C, Vázquez J, Domínguez J. A general model to estimate life in notches and fretting fatigue. Eng Fract Mech 2011;78(8):1590–601. https://doi.org/10.1016/j.engfracmech.2011.01.011.
[51] Vázquez J, Navarro C, Domínguez J. On the estimation of fatigue life in notches differentiating the phases of crack initiation and propagation. Fat. Fract. Eng. Mater Struct 2014;33(1):22–36. https://doi.org/10.1111/j.1460-2695.2009.01411.x.